nature water

Article

https://doi.org/10.1038/s44221-023-00079-4

Solar-driven efficient heterogeneous subminute water disinfection nanosystem assembled with fingerprint MoS_2

Received: 20 June 2022

Accepted: 10 April 2023

Published online: 18 May 2023

Check for updates

Tong Wu[1,4], Bofei Liu[1,4], Chong Liu[1], Jiayu Wan[1], Ankun Yang[1], Kai Liu[1], Feifei Shi[1], Jie Zhao[1], Zhiyi Lu[1], Guangxu Chen[1], Allen Pei[1], Harold Y. Hwang[2] & Yi Cui[1,3]

Although heterogeneous water disinfection can avoid secondary pollution and other shortcomings in homogeneous systems, its low disinfection efficiency seriously hinders its development. Here we successfully address the aforementioned issues of heterogeneous disinfection by developing discrete nanoflakes of $(Al_2O_3@v\text{-}MoS_2)/Cu/Fe_3O_4$. Three exciting features are integrated into such a novel structure: bifacial vertically aligned nanofingerprint MoS_2 grown on both sides of the light-transparent Al_2O_3 nanoflakes that can largely absorb sunlight, where both sides can operate simultaneously; a Cu-MoS_2 junction that enhances charge separation for the efficient generation of reactive oxygen species; and magnetic Fe_3O_4 nanoparticles that have magnetic separation capability and conveniently regenerate after disinfection. The $(Al_2O_3@v\text{-}MoS_2)/Cu/Fe_3O_4$ nanostructures reported herein exhibit outstanding water disinfection with thorough inactivation of over 5.7 $\log_{10}$ colony-forming units ml^{-1} *Escherichia coli* within 1 min in real sunlight (the system thermal effect has little impact on disinfection performances) as well as facile separation and stable long cycle reuse, demonstrating broad application prospects.

Approximately 30% of the world's population remains without access to safe drinking water, and 60% does not have access to safely managed sanitation services[1,2]. Waterborne diseases are responsible for 2 million deaths annually, and the majority of waterborne diseases occur in children under the age of 5 years[3–6]. Therefore, disinfection is very important and indispensable for domestic water safety. At present, the main disinfection technologies can be divided into three major categories: biological (for example, phage)[7], physical (for example, filtration, microwave, high temperature, plasma, ultraviolet (UV)-light irradiation and electroporation technologies)[8–11] and chemical (for example, potassium permanganate, halogenide agents, ozone, silver nanoparticles and titanium oxide) strategies[12–16]. Physical/biological methods other than UV-based technology are not widely used for large-scale water treatment because of their high energy consumption or long period needed for disinfection. UV and chemical methods have been the mainstream methods in this regard. Chemical disinfection can be divided into homogeneous and heterogeneous systems. Homogeneous systems mainly use effective collision at the molecular/ion scale as an advantage to achieve high-speed disinfection. However, they inevitably have secondary pollution risks of producing toxic residues and disinfection byproducts. Heterogeneous systems are relatively easy to separate and avoid the risk of toxicity. Their efficiencies are typically orders of magnitude lower than those of homogeneous systems because their number of contact active sites is small and the concentration of active

[1]Department of Materials Science and Engineering, Stanford University, Stanford, CA, USA. [2]Department of Applied Physics, Stanford University, Stanford, CA, USA. [3]Stanford Institute for Materials and Energy Sciences, SLAC National Accelerator Laboratory, Menlo Park, CA, USA. [4]These authors contributed equally: Tong Wu, Bofei Liu. e-mail: yicui@stanford.edu

products (for example, ROS) is not high enough. Attaining a high efficiency comparable to that of a homogeneous disinfector at a low cost and with no secondary pollution is a great challenge.

Heterogeneous catalytic disinfection mainly includes photocatalysis, electrocatalysis and thermal catalysis. The core mechanism of heterogeneous disinfection is to produce highly active oxidized substances to attack and destroy bacterial cell walls, cell membranes and DNA, leading to inactivation. Considering energy, efficiency, secondary pollution and other factors, photocatalytic disinfection has broader application prospects. There are two key factors that affect photocatalytic disinfection. First is about the reactive oxygen species (ROS) produced by photocatalyst. As early as 1985, scientists began to utilize the mechanism of TiO_2 photocatalysis to produce ROS for disinfection[17]. This work initially opened a new world of heterogeneous disinfection. However, there are many problems with this kind of research. For example, the utilization ratio of solar energy is low because the absorption spectrum of TiO_2 is mainly in the UV range. Therefore, visible-light-based catalytic disinfection has gradually become the focus[18]. Several types of visible light catalyst, such as nitrogen-doped TiO_2, graphite-phase carbon nitride, bismuth-based semiconductors and transition metal sulfide semiconductors, have been studied, and the catalytic efficiency of these visible-light catalysts has been improved by various synthesis and modification techniques. Some research relied on the heterojunction structures of $AgInS_2$-grown TiO_2 to expand the absorption wavelength to 700 nm, which made the disinfection efficiency over 10^3 times higher than TiO_2 but still cost 180 min (ref. 19). Graphitic carbon nitride (g-C_3N_4) is a novel metal-free polymeric photocatalyst with narrow bandgap energy of 2.7 eV. However, the photocatalytic efficiency of pure g-C_3N_4 is limited due to its fast recombination of photogenerated electron–hole pairs leading to low production of ROS. In some research, metallic Ag was used to promote the electron–hole pair separation of g-C_3N_4, which enhances the disinfection efficiency by 10^7 times taking 90 min (ref. 20). There has also been an effort to investigate the effect of g-C_3N_4 with different structures. As a result, the disinfection performance of g-C_3N_4 in two-dimensional (2D) structure is over 10^4 times better than that of g-C_3N_4 in bulk structure; even so, g-C_3N_4 in 2D structure still took 120 min to kill all *E. coli*[21]. However, their respective disadvantages are also very clear. The problem with type II heterojunctions is that the interfacial transfer of photogenerated electrons/holes sacrifices part of the oxidation capacity of the catalyst, and the interfacial transfer of photogenerated electrons/holes is inhibited by electrostatic action. The Schottky junction structure cannot adjust the bandgap or the position of the redox potential for producing more species of ROS and 2D semiconductor macroscopic materials greatly limit their lighting area and, more importantly, lead to the issue of poor contact probability with bacteria, which directly leads to a large waste of ROS due to the extremely short lifetimes and diffusion distance. In addition, the catalyst systems of *p*–*n* junctions and Schottky junctions are mostly discrete nanoparticles, and the issue of their efficient removal and recycling after disinfection has also been neglected. The current collection methods of heterogeneous sterilization are membrane separation and precipitation separation, but it is complicated, time consuming and difficult to reuse the catalysts, which results in high cost. Second is about the interaction between ROS and bacteria. It mainly involves the dispersion and collision of the catalytic disinfection system and the persistence of ROS attack on bacteria. Bacteria have high environmental adaptability and take various oxidative stress measures to cope with oxidative pressure, such as activating regulators to upregulate the synthesis of antioxidant enzymes and removing damaged biomacromolecules. In addition, bacteria have different ways of repairing DNA, lipid and protein damage. Therefore, only when increasing the bacterial contact rate with the catalyst and the ROS concentration to provide sustained ROS attack will the bacteria lose their regulatory ability and die. Recent research reported S vacancies in MoS_2 sheets. They can physically absorb and extract the lipids like a sharp knife, which helps the ·OH directly attack the DNA until death[22].

In summary, so far, heterogeneous disinfection is still far from achieving an efficiency comparable to that of homogeneous disinfection, let alone the integration of technology from disinfection to removal and recycling. To thoroughly solve the above problems, the following three points must be satisfied simultaneously in the design and preparation of this water disinfection system: (1) efficient visible-light catalytic conversion of high concentrations of ROS (chemical requirements), (2) large area for visible light absorption and large amount of close contact with bacteria (physical requirements) and (3) outstanding capability for removal and recycling (technological requirements).

In this Article, a visible-light ultrafast water-disinfection integrated system was synthesized by bifacial fingerprint multilevel assembly, which simultaneously realized ultraefficient transformation, diffusion and biological destruction triggered by photogenerating electrons/holes and ROS at the active sites, as well as rapid collection and recycling of the disinfection systems. We used Al_2O_3 nanoflakes as substrates to enable good dispersion and lighting effects due to their size and light transmission, respectively. Vertically aligned molybdenum sulfide (υ-MoS_2), which has broad visible light absorption, was grown on the surface of the Al_2O_3 nanoflakes as the catalyst for photocatalytic disinfection[23–31]. Copper particles were used to form the Schottky junction with υ-MoS_2 to accelerate electron–hole separation. Magnetic iron oxide particles were coated on the catalyst surface by electrostatic adsorption so that the catalyst could be collected by a magnet after usage. Our multifeature structural design exhibited a high inactivation efficiency for 5.7 log colony-forming units (CFU) cm^{-1} *Escherichia coli* within a very short time of 1 min under natural sunlight irradiation, which will facilitate revolutionary changes in water disinfection.

Design of the heterogeneous disinfection system

Figure 1a shows the schematic synthesis process of the (Al_2O_3@υ-MoS_2)/Cu/Fe_3O_4 multifeature particles. A fingerprint-like MoS_2 film with a vertically aligned layered structure was grown on the surface of Al_2O_3 nanoflakes based on the high-temperature sulfuration of MoO_x. The thickness of MoS_2 was determined by the MoO_x thickness, which was controllable by the concentration of molybdate precursor (Supplementary Fig. 1). Afterward, the metal copper was uniformly coated on top of the MoS_2 layer via a disproportionation reaction. Magnetic nanoparticles were assembled on the surface of MoS_2. Figure 1b illustrates the ROS generation process under sunlight. As a sunlight photon harvester, the vertical-MoS_2 (υ-MoS_2) material has electrons that can be easily excited. The electron–hole pairs are separated and transported along the vertical MoS_2 to their edges to participate in ROS generation with water and dissolved oxygen. ROS radicals, such as superoxide, hydrogen peroxide and singlet oxygen, are produced and released from the MoS_2 nanoflakes into water to inactivate bacteria. Due to the short lifetime of ROS radicals, the ROS mainly concentrate at regions adjacent to the nanoflakes (the shortest ROS diffusion distance was calculated within 4 nm, as shown in Supplementary Table 1). Figure 1c shows all the details of our process. The (Al_2O_3@υ-MoS_2)/Cu/Fe_3O_4 particles were dispersed in bacteria-contaminated water, and ROS radicals were produced around the nanoflakes (yellow halo in Fig. 1c) when the particles were exposed to sunlight. After the disinfection process was finished, the nanoflakes in the water were fully extracted with a magnetic separation approach and employed for the next cycle. It is noteworthy that because the nanoflakes were suspended and well dispersed in the solution, this design increased the collision possibility of the (Al_2O_3@υ-MoS_2)/Cu/Fe_3O_4 particles with bacteria.

Preparation and characterization of (Al_2O_3@υ-MoS_2)/Cu

Compared with the traditional synthesis of 2D materials on a large silicon wafer or glassy carbon, it is challenging to achieve a uniform metal coating on a powder substrate with conventional metal coating methods, such as evaporation and sputtering. Here we applied the

https://doi.org/10.1038/s44221-023-00079-4

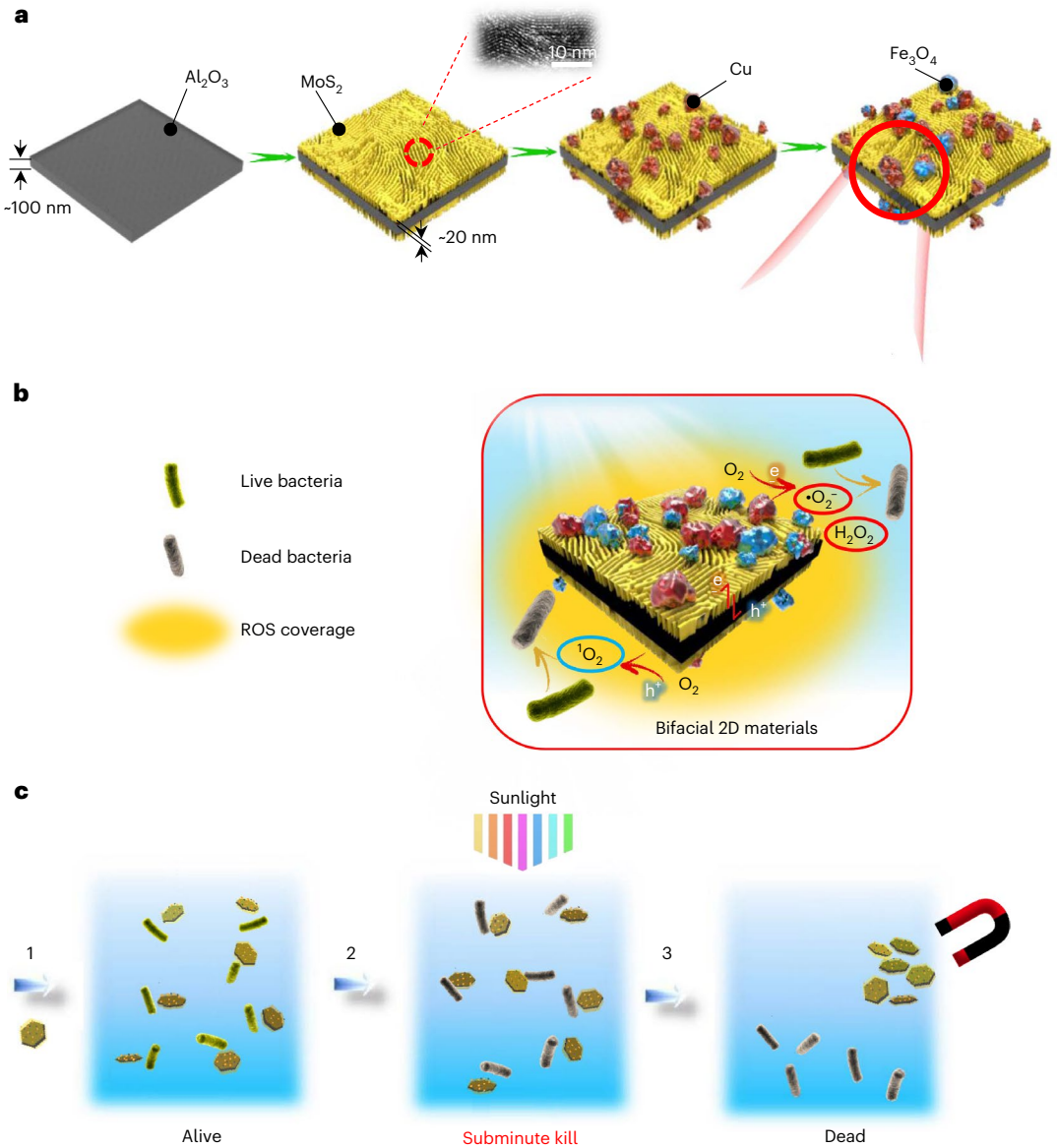

Fig. 1 | The synthesis and disinfection operation schematic of (Al_2O_3@*v*-MoS_2)/Cu/Fe_3O_4. a, Step-by-step synthesis of (Al_2O_3@*v*-MoS_2)/Cu/Fe_3O_4. The preparation methods include surface adsorption, chemical vapour deposition, planting and charge neutralization. **b**, Scheme of photocatalytic ROS with sunlight. The yellow halo represents valid ROS coverage. Under sunlight, the upper edges of MoS_2 can release electrons to obtain superoxide, hydroxyl radical and hydrogen peroxide. The photogenerated holes can spread to the edges near the bottom of MoS_2. By recombination with the produced superoxide radical, electron transfer occurs and the superoxide radical is oxidized to singlet oxygen. All these ROS can destroy the cell membranes of bacteria and kill them rapidly. **c**, Schematic representation of cyclic utilization for water disinfection (1, dispersion; 2, irradiation; 3, collection).

surface wetting method with molybdate to overcome this challenge[32]. After wetting and dehydration, the surface of the Al_2O_3 nanoflakes was coated with a thin molybdate film. The Al_2O_3 nanoflake powder was heated to over 550 °C with sulfur gases and then cooled quickly to room temperature. This process produced a multilayer vertically aligned MoS_2 film on the surface of Al_2O_3 (refs. 33,34). Cu nanoparticles were deposited by first immersing the Al_2O_3@*v*-MoS_2 into cuprous saline solution, followed by heating to cause a disproportionation reaction[35].

We carried out scanning electron microscopy (SEM) and transmission electron microscopy (TEM) characterizations of the materials to study their unique material structure. As illustrated in Fig. 2a and Supplementary Fig. 3, the individual construction was biscuit-like with a diameter of 5–10 μm and a thickness of 100–150 nm. TEM images of the edge (iii) and centre (iv) suggest that our fabricated MoS_2 film had a compact multilayer structure that showed a vertically aligned morphology with a layer spacing of 0.72–0.75 nm and 12–18 stacked layers. The vertically grown molybdenum sulfide obtained by this new synthesis method had more continuous molybdenum sulfide stacked layers[34,35]. This change in the layers further increased the active edges of molybdenum sulfide, which is more conducive to ROS generation and diffusion. It should be noted that this vertically aligned structure can expose electrochemically active edge sites, minimize the transport length (vertical thickness of film) of carriers at the reaction sites and thus enhance the ROS yield. X-ray photoelectron spectroscopy (XPS) was used to confirm the components of the MoS_2 material. As shown in Fig. 2b, the signals of Mo^{4+}, S^{2-} and Al^{3+} clearly appeared at 413.3, 395.3, 232.3, 229.4, 164.4, 163.2 and 120.2, and 75.3 eV, respectively. After plating Cu°, a small peak appeared at 933.8 eV, and the valence state was further indicated by Auger electron spectroscope (AES) (Supplementary Figs. 4 and 5). Cu metal can form a Schottky junction

https://doi.org/10.1038/s44221-023-00079-4

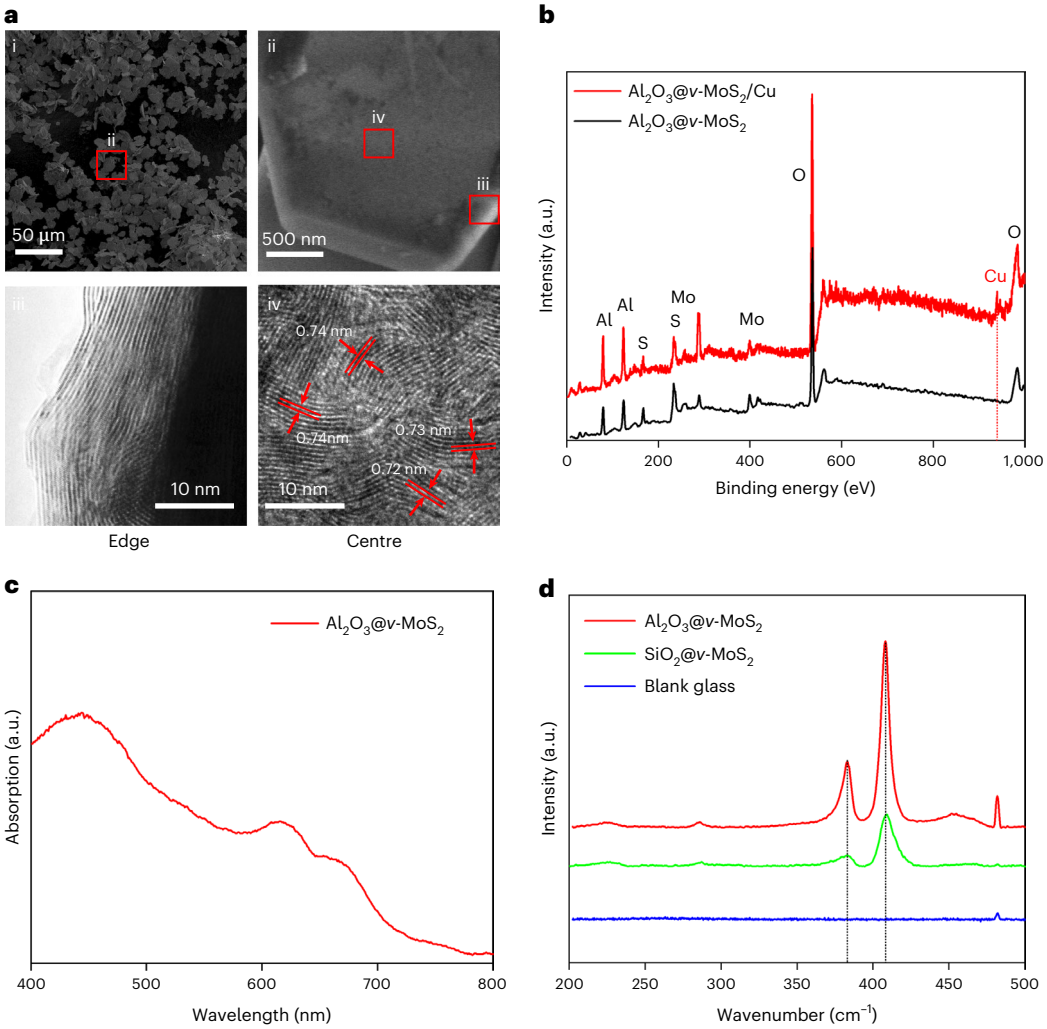

Fig. 2 | Characterizations of Al_2O_3@*v*-MoS_2 and (Al_2O_3@*v*-MoS_2)/Cu. a, SEM (i and ii) and TEM (iii and iv) images showing the morphologies and secondary structure of (Al_2O_3@*v*-MoS_2)/Cu. The red boxes indicate the enlarged individual area (ii) or regions (iii, iv). The as-grown MoS_2 film is composed of vertically aligned layers of MoS_2 with domain sizes of approximately 12–18 layers. The spacing between two vertical layers is approximately 0.72–0.75 nm. **b**, Full XPS spectra of (Al_2O_3@*v*-MoS_2)/Cu. **c**, UV–Vis absorption spectra of Al_2O_3@*v*-MoS_2. The cut-off wavelength of Al_2O_3@*v*-MoS_2 is approximately 750 nm, whereas Al_2O_3 has no absorption ($P = 1.5 \times 10^{-3}$ mg l^{-1}). **d**, Raman spectra of horizontal MoS_2 and Al_2O_3@*v*-MoS_2. The E^1_{2g} peak of *v*-MoS_2 is approximately one-third of the A^1_g peak.

with the MoS_2 film to separate electron–hole carriers for efficient ROS production. The absorption wavelength is one of the most important parameters. To prove that our as-prepared material has visible light absorption, its ultraviolet–visible (UV–Vis) absorption spectrum was measured. The bandgap was characterized by measuring the UV–Vis absorption spectrum of Al_2O_3@*v*-MoS_2 (Fig. 2c and Supplementary Fig. 6). The bandgap value (E_g) of this indirect bandgap semiconductor was extracted from the relation between the absorption coefficient and photon energy. The Tauc plot ($(\alpha h\nu)^{1/2}$ versus $h\nu$) derived from this absorption spectrum is shown in Supplementary Fig. 7. The bandgap energy gives 1.56 eV for Al_2O_3@*v*-MoS_2 which allows it to absorb light up to 750 nm wavelength. This suggests that Al_2O_3@*v*-MoS_2 is fully capable of absorbing all wavelengths of visible light (400–700 nm). The valence band position (E_v) of Al_2O_3@*v*-MoS_2 was confirmed as 5.56 eV using UV photoelectron spectroscopy, and the results are shown in Supplementary Fig. 8. Therefore, the band position of Al_2O_3@*v*-MoS_2 gives a conduction band minimum (4.00 eV, −0.44 eV versus normal hydrogen electrode (NHE)) and valance band maximum (5.56 eV, 1.12 eV versus NHE), which fully overlap with the oxygen reduction potentials $O_2/{\cdot}O_2^-$ (4.11 eV, −0.33 eV versus NHE) and O_2/H_2O_2 (4.72 eV, 0.28 eV versus NHE) and water oxidation potentials $H_2O/{}^1O_2$ (5.26 eV, 0.82 eV versus NHE). It is clear that Al_2O_3@*v*-MoS_2 is the most suitable for ROS generation for photocatalytic water disinfection. The Raman spectrum in Fig. 2d was further characterized to confirm this vertically aligned structure. Two strong peaks at 408 and 383 cm^{-1} and one weak peak at 285 cm^{-1} were detected, contributing to the E^1_{2g}, A^1_g and E_{1g} peaks, respectively. Bulk MoS_2, however, had no peak at 285 cm^{-1} because the E_{1g} mode is forbidden in the backscattering experiment on the basal plane (Supplementary Fig. 10). This result suggested the vertically aligned structure of MoS_2 in Al_2O_3@*v*-MoS_2 (ref. 36).

Photocatalytic disinfection performance

All disinfection tests were performed with suspensions of the Gram-negative bacterium *E. coli*. The original bacterial concentration was approximately 10^5–10^6 CFU ml^{-1}. We first investigated whether MoS_2 nanoflakes can effectively work as photocatalysts under visible light. Figure 3a compares the inactivation efficiency of bacteria with Al_2O_3@*v*-MoS_2 in the dark and under illumination, together with the blank water in light. Sunlight was generated by a solar simulator equipped with a 400 nm cut-off UV filter (Supplementary Fig. 11) to

https://doi.org/10.1038/s44221-023-00079-4

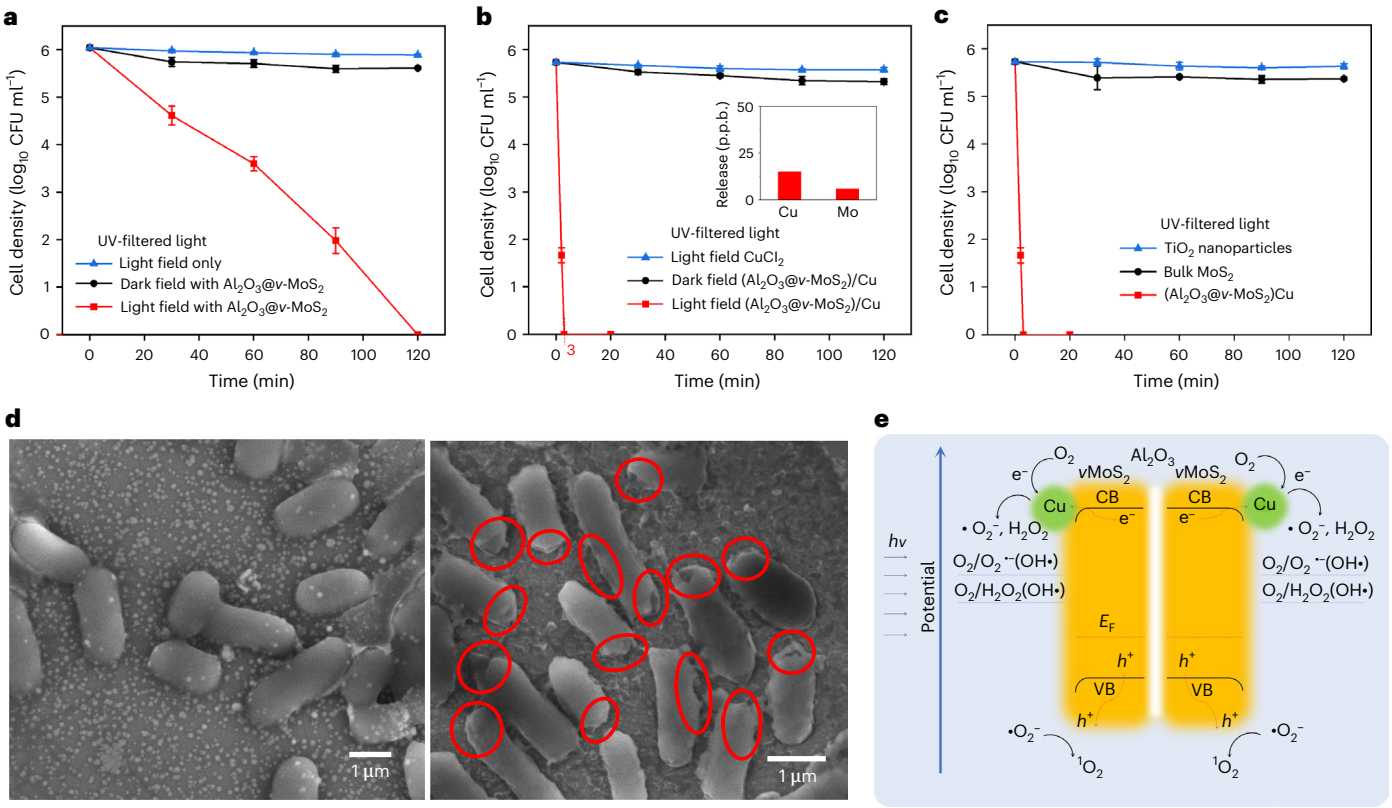

Fig. 3 | Disinfection performance and principle of (Al_2O_3@v-MoS_2)/Cu system. **a**, Disinfection performance comparison of Al_2O_3@v-MoS_2 in a dark/light field and blank *E. coli* in a light field showing that the disinfection of Al_2O_3@v-MoS_2-based nanoscavengers is a light-driven catalytic reaction process. **b**, Comparison of the disinfection performances of (Al_2O_3@v-MoS_2)/Cu in the dark/light showing the great promotion after Cu plating and that of Cu^{2+} in the light field to prove the lower antibacterial effect. Inset shows Cu^{2+} release during disinfection by ICP–MS. **c**, Comparison of the disinfection performance of TiO_2 nanoparticles, bulk MoS_2 and (Al_2O_3@v-MoS_2)/Cu. In **a**–**c**, the data are presented as mean ± s.d ($n = 3$). **d**, SEM images of solution samples (*E. coli*) separated at low speed before and after disinfection. After disinfection, the cell membrane was seriously damaged, as shown in red circles. **e**, Schematic representation of photocatalysis with the bifacially structured (Al_2O_3@v-MoS_2)/Cu; CB indicates conduction band and VB indicates valence band. The point at 0 CFU ml^{-1} indicates that all the *E. coli* cells are dead. Experimental conditions: $T = 25$ °C, $[pH]_0$ 6.5 and initial concentrations of *E. coli* of $10^{6.04}$ CFU ml^{-1} (**a**) and $10^{5.73}$ CFU ml^{-1} (**b** and **c**).

suppress the UV disinfection effect. Under filtered light irradiation, compared with the weak disinfection effect in the blank sample, the disinfection effect of Al_2O_3@v-MoS_2 was strong, with all of *E. coli* successfully inactivated within 2 h by Al_2O_3@v-MoS_2, after which live bacteria could not be detected (Supplementary Fig. 12). This control test confirmed that the disinfection effect of our Al_2O_3@v-MoS_2 did not originate from the natural death of bacteria under light. The 2 h disinfection time of 'naked' MoS_2 nanoflakes is still too long for practical applications. To speed up this process, we introduced copper metal particles on the MoS_2 film to form the (Al_2O_3@v-MoS_2)/Cu composite. After coating the copper nanoparticles, a 40-times-shorter disinfection time was achieved. As demonstrated in Fig. 3b, an inactivation of 5.73 log_{10} CFU ml^{-1} *E. coli* was acquired after the 3 min disinfection process of (Al_2O_3@v-MoS_2)/Cu in comparison with that acquired after the 2 h disinfection process of Al_2O_3@v-MoS_2 (Fig. 3a). To the best of our knowledge, no reported photocatalysts have achieved such a remarkable inactivation speed. We also compared the performance of our catalyst with that of simply adding Cu^{2+} ions to exclude the effect of Cu^{2+} ion release. To this end, $CuCl_2$ (10 p.p.m.) was added for comparison. It can be clearly seen that no disinfection effect was found for the sample with only Cu^{2+} ions, suggesting that our observed disinfection effect for (Al_2O_3@v-MoS_2)/Cu was not caused by the released Cu^{2+} ions. We carried out inductively coupled plasma–mass spectrometry (ICP–MS) measurements to measure the Cu release. The inset of Fig. 3b shows that less than 20 p.p.b. Cu^{2+} was released into the water from Cu^0 during the visible photocatalysis process, which is much lower than the safe drinking level of 1.3 p.p.m. A comparison of the (Al_2O_3@v-MoS_2)/Cu nanoflakes with well-studied TiO_2 nanoparticles and bulk MoS_2 was further performed under similar experimental conditions (Fig. 3c). TiO_2 nanoparticles under UV-filtered light showed an extremely weak disinfection performance (5.60 log_{10} CFU ml^{-1} *E. coli* remaining alive after 2 h) because of their limited capacity to absorb photons in the visible spectrum. Bulk-type MoS_2 also displayed a lower disinfection effect (5.37 log_{10} CFU ml^{-1} *E. coli* remaining alive after 2 h) in comparison with its nanoflake counterpart. This clearly verified the notable role of the 2D MoS_2 material structure design in the disinfection process.

Photocatalytic antibacterial mechanism of (Al_2O_3@v-MoS_2)/Cu

After low-speed centrifugation, samples of supernatant were further observed by SEM. The *E. coli* cells detected before and after disinfection (3 min) with (Al_2O_3@v-MoS_2)/Cu were obviously different in terms of the edge integrity (Fig. 3d). The wall of Gram-negative bacteria (such as *E. coli*) contains a thin peptidoglycan layer for self-protection. We found many irregularly shaped damage areas all around the cells (Supplementary Fig. 13). As shown in Fig. 3d, the original cells had a smooth appearance, whereas their appearance was badly destroyed everywhere after disinfection, and most of the fimbriae fell off. This is because the high concentrations of ROS produced by photocatalysis reacted with the double bonds of the peptidoglycan layer and penetrated into the bacteria, changing the membrane permeability and leading to bacterial death.

https://doi.org/10.1038/s44221-023-00079-4

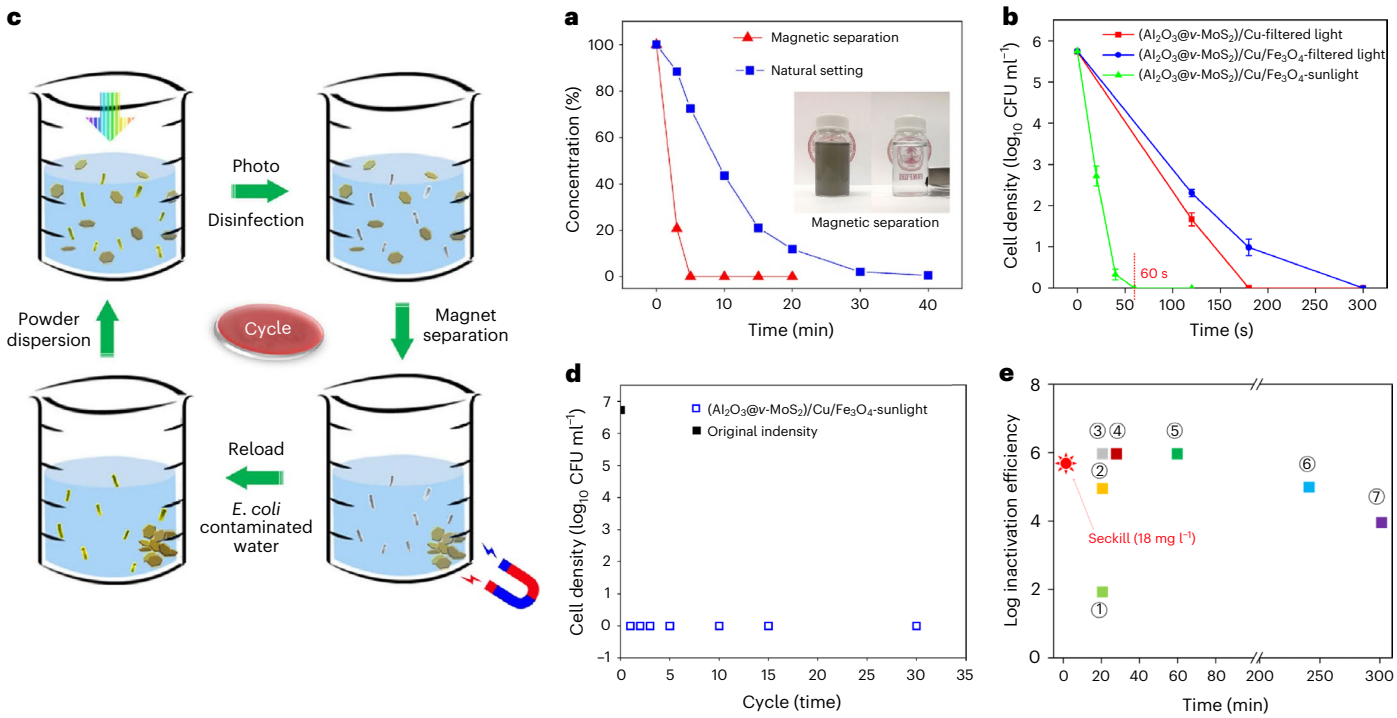

Fig. 4 | Recyclable subminute sunlight disinfection of (Al_2O_3@v-MoS_2)/Cu/Fe_3O_4. a, Magnetic separation experiment showing the relative concentration change in the supernatant with separation time calculated by spectrophotometry data. Comparison of magnetic separation and natural settling. **b**, Comparison of the disinfection performance of (Al_2O_3@v-MoS_2)/Cu and (Al_2O_3@v-MoS_2)/Cu/Fe_3O_4 under different light sources. After magnetic modification, (Al_2O_3@v-MoS_2)/Cu/Fe_3O_4 has scarcely any decay compared with (Al_2O_3@v-MoS_2)/Cu. In real sunlight, a thorough disinfection with (Al_2O_3@v-MoS_2)/Cu/Fe_3O_4 is completed in 60 s (sec-kill). The point at 0 CFU ml^{-1} indicates that all the *E. coli* cells are dead. Experimental conditions: T = 25 °C, $[pH]_0$ 6.5 and initial concentrations of *E. coli* of $10^{5.74}$ CFU ml^{-1}; the data are presented as mean ± s.d. (n = 3). **c**, Illustration of the multicyclic system. **d**, Cyclic system proving the stability of (Al_2O_3@v-MoS_2)/Cu/Fe_3O_4. **e**, Disinfection performance comparison of (Al_2O_3@v-MoS_2)/Cu/Fe_3O_4 with other photocatalysts reported in the literature using *E. coli*. Red sun (this work), ① (ref. 19), ② (ref. 30), ③ (ref. 39), ④ (ref. 41), ⑤ (ref. 21), ⑥ (ref. 43), ⑦ (ref. 42).

The inactivation mechanism of (Al_2O_3@v-MoS_2)/Cu is illustrated in Fig. 3e. Cu metal adhering on Al_2O_3@v-MoS_2 formed a metal/semiconductor junction with the interfacial band bent down. Once the photons were harvested by Al_2O_3@v-MoS_2 materials, electrons and holes were excited, separated, and transported to both sides of Al_2O_3 for ROS generation. Then, for the existing Schottky junction from the Cu/v-MoS_2 composite, the bent conduction band facilitated electron transport easily to the active sites on the vertical edges of MoS_2 for ROS production. This is also the origin of the disinfection speed difference between the Al_2O_3@v-MoS_2 and (Al_2O_3@v-MoS_2)/Cu materials. The separated electrons on Cu reduced O_2 into $O_2^{\bullet-}$ and H_2O_2. On the MoS_2 side, O_2 transformed into its excited $^1O_2$ state with the help of holes. The generation of ROS was further confirmed by a scavenger quenching test. Masking agents, including TEPO, L-histidine, catalase and isopropanol, were selected to quench the generated ROS species, as demonstrated in Supplementary Fig. 14. When a masking agent is used to react with one of the active oxygen species, if the disinfection effect is greatly reduced, it indicates that the active oxygen species should be the main disinfection contributor with a high concentration produced by photocatalysis. The experimental results showed that singlet oxygen, hydroxyl radicals, superoxide radicals and hydrogen peroxide obviously reduced the bactericidal effect after quenching. This proved that all four ROSs were expressed in the (Al_2O_3@v-MoS_2)/Cu system. Their strong signals were all detected by electron paramagnetic resonance, which proved this conclusion (Supplementary Fig. 17). As shown in Supplementary Fig. 14, with the addition of TEMPO or catalase, around 3 log_{10} or 4 log_{10} CFU ml^{-1} of *E. coli* could be killed, respectively. However, only around 2 log_{10} CFU ml^{-1} of *E. coli* could be killed with the addition of isopropanol and L-histidine. The scavenging effect from high to low in the (Al_2O_3@v-MoS_2)/Cu system according to the reaction rate was in the order of isopropanol (for ·OH), L-histidine (for $^1O_2$), TEMPO (for $\cdot O_2^-$) and catalase (for H_2O_2). These results indicated that the ·OH and $^1O_2$ are major ROSs for our photocatalytic disinfection system because of having a much higher redox potential (·OH: 2.80 V, $^1O_2$: 1.88 V).

On the other hand, as shown in Supplementary Table 1, the lifetimes of singlet oxygen and hydroxyl radicals were much lower than those of superoxide radicals and hydrogen peroxide, and the diffusion distances were also extremely short. Therefore, the advantage of our disinfection system lies in that, on the basis of achieving a high ROS output through a 2D structure, good dispersion can also be achieved to facilitate full contact with *E. coli*, thus realizing the full use of hydroxyl radicals and singlet oxygen. Therefore, they are two of the most important disinfection ROSs in the scavenger quenching test. In the discrete 2D system of this work, four ROSs are not only maximized by the vertically grown 2D structure of molybdenum sulfide but also provide the necessary bacterial contact probability due to the dispersion of the substrate.

Magnetic functionalization and subminute disinfection

The separation/collection of photocatalysts is a general issue for heterogeneous water treatment processes. Here we overcame this problem by applying magnetic modification to (Al_2O_3@v-MoS_2)/Cu materials[37]. As demonstrated in Fig. 1c, anionic surfactant-wrapped Fe_3O_4 nanoparticles of 10–15 nm were easily attached to Al_2O_3 nanoflakes with positive surface charges, as shown in Supplementary Fig. 15. Figure 4a shows the concentration versus time curves with magnetic and gravity separation approaches. We observed that our magnetic separation approach was

very effective and required only 5 min to completely remove our catalyst from the solution, which is eight times faster than natural settling.

The illuminated disinfection performance of (Al_2O_3@υ-MoS_2)/Cu and (Al_2O_3@υ-MoS_2)/Cu/Fe_3O_4 under UV-filtered light is further compared in Fig. 4b. It can be clearly seen that, even with the magnetic particles on (Al_2O_3@υ-MoS_2)/Cu, the disinfection curves were still comparable for the (Al_2O_3@υ-MoS_2)/Cu (3 min for 5.7 log inactivation efficiency) and (Al_2O_3@υ-MoS_2)/Cu/Fe_3O_4 (5 min for 5.7 log inactivation efficiency) samples, demonstrating that the coating of magnetic particles had no significant detrimental effect on the disinfection efficiency. The minimal difference between (Al_2O_3@υ-MoS_2)/Cu and (Al_2O_3@υ-MoS_2)/Cu/Fe_3O_4 originated from the Fe_3O_4 particles shading the incident light. Note that these magnetic particles were 10 nm in size, and the 2% mass loading was extremely low.

We further carried out the disinfection test in real sunlight (14:00 local time, 5 July 2018, Stanford, CA, USA; Supplementary Fig. 16) to prove the material's adaptivity and potential in real applications, and the disinfection performance of (Al_2O_3@υ-MoS_2)/Cu/Fe_3O_4 under simulated and real sunlight are compared in Fig. 4b. A 5.7 log inactivation efficiency was achieved in real sunlight, and no live bacteria were detected within 60 s. Such high-speed disinfection under sunlight is probably the best among that of all heterogeneous disinfection materials. The improvement under sunlight compared with UV-filtered light was due to the participation of additional UV light absorption and direct disinfection processes. The stability of the materials was proven over 30 times, and the full disinfection steps of every cycle process are schematically demonstrated in Fig. 4c, including the CFUs of live *E. coli* cells for the 1st, 2nd, 3rd, 5th, 10th, 15th and 30th cycles counted after incubation. As shown in Fig. 4d, over 5.7 $\log_{10}$ CFU ml^{-1} *E. coli* inactivation was achieved within 60 s even for the 30th cycle. This observation indicated that (Al_2O_3@υ-MoS_2)/Cu/Fe_3O_4 is very stable against possible damage by ROS.

The disinfection efficiency comparison of our nanoscavenger (Al_2O_3@υ-MoS_2)/Cu/Fe_3O_4 with other top photocatalytic materials was performed on the basis of a review of the literature in terms of the speed and log inactivation concentration of bacteria[19–21,29–31,38–43]. For an over 2 log inactivation, we found no other photocatalytic material that provides a disinfection efficiency as high as this work within 60 s (Fig. 4e). Not only is this the best efficiency, but the mass loading (~18 mg l^{-1}) is also much lower than that in previous reports.

Conclusion

In this work, Al_2O_3@υ-MoS_2-based magnetically photoresponsive nanoscavengers, which can fully harvest UV and visible light under real sunlight, are prepared and deployed for water cyclic disinfection. Using a 2D vertically aligned MoS_2 film can shrink the bandgap and extend its absorption cut-off to 800 nm so that it can make full use of solar energy during photocatalytic disinfection. Four kinds of ROS, which can strongly destroy the peptidoglycan layer outside bacterial cells, can be detected in this process. Plating Cu particles lowers the energy barrier of electron escape to accelerate electron transport. After 3 min of irradiation, (Al_2O_3@υ-MoS_2)/Cu shows a 5.7 log inactivation of bacterial concentration. Using a charge-attract reaction, the magnetic particles can be easily modified on the (Al_2O_3@υ-MoS_2)/Cu surface, which makes it possible to collect the catalysts by magnet. This final material (Al_2O_3@υ-MoS_2)/Cu/Fe_3O_4 not only achieves a thorough inactivation of over 5.7 $\log_{10}$ CFU ml^{-1} *E. coli* within 60 s under real sunlight irradiation but also demonstrates exceptional stability after repeated usage. We believe that our catalyst design represents state-of-the-art photodisinfection and will inspire more innovations in this exciting interdisciplinary field.

Methods

Preparation of (Al_2O_3@υ-MoS_2)/Cu/Fe_3O_4

The Al_2O_3 nanoflakes were stirred in a solution of 2 g ammonium molybdate with 15 g water. After ultrasonication, the suspended Al_2O_3 was collected by filtration and washed three times with distilled water. After drying at 80 °C, the sulfuration of the powder was quickly performed by chemical vapor deposition (CVD), as shown in Supplementary Fig. 2b. The sulfur was placed in an alumina boat upstream. The temperature of the furnace was first ramped up to 550 °C in 15 min, then this temperature was maintained for another 10 min for growth. The sulfur temperature was approximately 200 °C. Then, the colour of the powder turned from white to grey. The grey powder (300 mg) was suspended in an acetone solution (100 ml) of tetrakis(acetonitrile) copper(I)hexafluorophosphate (50 mg). The reaction took place at 50 °C for 30 min. After the reaction, the substrate was further rinsed in hot acetone and then dried in air to obtain (Al_2O_3@υ-MoS_2)/Cu (ref. 35). Magnetization was performed by dropping diluted ferrofluid solution into suspended water with (Al_2O_3@υ-MoS_2)/Cu, stirring overnight and then filtrating, washing and drying to obtain (Al_2O_3@υ-MoS_2)/Cu/Fe_3O_4 as ash black powder.

Disinfection performance characterization

E. coli (JM109, Promega) bacteria were cultured to log phase (10^9 CFU ml^{-1} after 4–6 h), collected via centrifugation ((Al_2O_3@υ-MoS_2)/Cu/Fe_3O_4 collected via magnetic field), washed three times with phosphate-buffered saline (Thermo Fisher Scientific) solution and dispersed in 200 ml de-ionized water to an initial bacteria concentration of ~10^6 CFU ml^{-1}. A solar simulator (Newport, Class AAA) with a simulated air mass 1.5 (AM 1.5, 100 mW cm^{-2}) output was adopted as the light source in the solar water disinfection experiments. The AM 1.5 light power (1 sun) was calibrated to 100 mW cm^{-2} using a certified monocrystalline silicon solar cell before real characterizations. UV (Clarex) light was adopted to modulate the 1-sun light spectrum according to the experimental requirements. The disinfection materials were dispersed in 25 ml of *E. coli* simulated water and sampled under irradiation with a UV-filtered light source at different intervals. The bacterial concentrations of samples under illumination and baseline (without disinfection) conditions were measured using standard spread plating techniques. The magnetically separated sampled water samples were serially diluted, and each dilution was plated in triplicate onto trypticase soy agar (Bacto) and incubated at 37 °C for 16–18 h. Water disinfection experiments in the dark were also carried out with the same process in a dark environment. Disinfected and baseline samples were compared to determine the disinfection performance of the disinfection devices.

Data availability

All data of this study are presented in the article and its supplementary information. Source data are provided with this paper. The source data and relevant data that support the findings can also be accessed through the figshare repository and are freely available for download (https://doi.org/10.6084/m9.figshare.22094465).

References

1. Ferraro, P. J. & Prasse, C. C. Reimagining safe drinking water on the basis of twenty-first-century science. *Nat. Sustain.* **4**, 1032–1037 (2021).
2. Chu, C., Ryberg, E. C., Loeb, S. K., Suh, M.-J. & Kim, J.-H. Water disinfection in rural areas demands unconventional solar technologies. *Acc. Chem. Res.* **52**, 1187–1195 (2019).
3. World Health Organization. *Waterborne disease related to unsafe water and sanitation*. http://www.who.int/sustainable-development/housing/health-risks/waterborne-disease/en/ (2018).
4. Chen, Y. et al. Advanced oxidation processes for water disinfection: features, mechanisms and prospects. *Chem. Eng. J.* **409**, 128207–128228 (2021).
5. La Rosa, G., Bonadonna, L., Lucentini, L., Kenmoe, S. & Sufredini, E. Coronavirus in water environments: pccurrence, persistence and concentration methods—a scoping review. *Water Res.* **179**, 115899 (2020).

6. Bogler, A. et al. Rethinking wastewater risks and monitoring in light of the COVID-19 pandemic. *Nat. Sustain.* **3**, 981–990 (2020).
7. Mathieu, J., Yu, P., Zuo, P., Da Silva, M. L. B. & Alvarez, P. J. J. Going viral: emerging opportunities for phage-based bacterial control in water treatment and reuse. *Acc. Chem. Res.* **52**, 849–857 (2019).
8. Zhang, J. L. et al. Guanidyl-functionalized graphene/polysulfone mixed matrix ultrafiltration membrane with superior permselective, antifouling and antibacterial properties for water treatment. *J. Colloid Interface Sci.* **540**, 295–305 (2019).
9. Chen, W. et al. Silver nanowire-modified filter with controllable silver ion release for point-of-use disinfection. *Environ. Sci. Technol.* **53**, 7504–7512 (2019).
10. Lee, H. R. et al. Antimicrobial effects of microwave plasma-activated water with skin protective effect for novel disinfectants in pandemic era. *Sci. Rep.* **12**, 5968–5981 (2022).
11. Zhang, S. H., Ye, C. S., Lin, H. R., Lv, L. & Yu, X. UV disinfection induces a VBNC state in *Escherichia coli* and *Pseudomonas aeruginosa*. *Environ. Sci. Technol.* **49**, 1721–1728 (2015).
12. Atkinson, A. J., Apul, O. G., Schneider, O., Garcia-Segura, S. & Westerhoff, P. Nanobubble technologies offer opportunities to improve water treatment. *Acc. Chem. Res.* **52**, 1196–1205 (2019).
13. Pak, G. et al. Comparison of antibiotic resistance removal efficiencies using ozone disinfection under different pH and suspended solids and humic substance concentrations. *Environ. Sci. Technol.* **50**, 7590–7600 (2016).
14. Yan, H. et al. Recyclable and reusable direct Z-scheme heterojunction CeO_2/TiO_2 nanotube arrays for photocatalytic water disinfection. *Appl. Catal. B* **291**, 120096–120104 (2021).
15. Hindiyeh, M. & Ali, A. Investigating the efficiency of solar energy system for drinking water disinfection. *Desalination* **259**, 208–215 (2010).
16. McGuigan, K. G. et al. Solar water disinfection (SODIS): a review from bench-top to roof-top. *J. Hazard. Mater.* **235–236**, 29–46 (2012).
17. Matsunaga, T., Tomoda, R., Nakajima, T. & Wake, H. Photoelectrochemical disinfection of microbial cells by semiconductor powders. *FEMS Microbiol. Lett.* **29**, 211–214 (1985).
18. Fernandez-Ibanez, P. et al. Solar photocatalytic disinfection of water using titanium dioxide graphene composites. *Chem. Eng. J.* **261**, 36–44 (2015).
19. Du, J. et al. Uncovering the mechanism of novel $AgInS_2$ nanosheets/TiO_2 nanobelts composites for photocatalytic remediation of combined pollution. *Appl. Catal. B* **259**, 118062 (2019).
20. Ma, S. L., Zhan, S. H., Jia, Y. N., Shi, J. & Jia, Q. X. Enhanced disinfection application of Ag-modified g-C_3N_4 composite under visible light. *Appl. Catal. B* **186**, 77–87 (2016).
21. Teng, Z. et al. Edge-functionalized g-C_3N_4 nanosheets as a highly efficient metal-free photocatalyst for safe drinking water. *Chem* **5**, 664–680 (2019).
22. Wang, J. et al. 'Nano Killers' activation by permonosulfate enables efficient anaerobic microorganisms disinfection. *J. Hazard. Mater.* **440**, 129742 (2022).
23. Lopez-Sanchez, O., Lembke, D., Kayci, M., Radenovic, A. & Kis, A. Ultrasensitive photodetectors based on monolayer MoS_2. *Nat. Nanotechnol.* **8**, 497–501 (2013).
24. Xia, F., Wang, H., Xiao, D., Dubey, M. & Ramasubramaniam, A. Two dimensional material nanophotonics. *Nat. Photon.* **8**, 899–907 (2014).
25. Gong, Y. J. et al. Vertical and in-plane heterostructures from WS_2/MoS_2 monolayers. *Nat. Mater.* **13**, 1135–1142 (2014).
26. Zhang, J. S. et al. Reversible and selective ion intercalation through the top surface of few-layer MoS_2. *Nat. Commun.* **9**, 5289–5297 (2018).
27. Wang, H., Yuan, H., Hong, S. S., Li, Y. & Cui, Y. Physical and chemical tuning of two-dimensional transition metal dichalcogenides. *Chem. Soc. Rev.* **44**, 2664–2680 (2015).
28. Jaramillo, T. F. et al. Identification of active edge sites for electrochemical H_2 evolution from MoS_2 nanocatalysts. *Science* **317**, 100–102 (2007).
29. Mak, K. F., Lee, C., Hone, J., Shan, J. & Heinz, T. F. Atomically thin MoS_2: a new direct-gap semiconductor. *Phys. Rev. Lett.* **105**, 136805–136808 (2010).
30. Liu, C. et al. Rapid water disinfection using vertically aligned MoS_2 nanofilms and visible light. *Nat. Nanotechnol.* **11**, 1098–1104 (2016).
31. Attri, P. et al. Generation mechanism of hydroxyl radical species and its lifetime prediction during the plasmainitiated ultraviolet (UV) photolysis. *Sci. Rep.* **5**, 9332–9339 (2015).
32. Deng, J. et al. Multiscale structural and electronic control of molybdenum disulfide foam for highly efficient hydrogen production. *Nat. Commun.* **8**, 14430–14438 (2017).
33. Kong, D. et al. Synthesis of MoS_2 and $MoSe_2$ films with vertically aligned layers,. *Nano Lett.* **13**, 1341–1347 (2013).
34. Wang, H. et al. Electrochemical tuning of vertically aligned MoS_2 nanofilms and its application in improving hydrogen evolution reaction,. *Proc. Natl Acad. Sci. USA* **110**, 19701–19706 (2013).
35. Gong, Y. et al. Spatially controlled doping of two-dimensional SnS_2 through intercalation for electronics. *Nat. Nanotechnol.* **13**, 294–299 (2018).
36. Zhu, G. et al. Tuning thermal conductivity in molybdenum disulfide by electrochemical intercalation,. *Nat. Commun.* **7**, 13211–13220 (2016).
37. Erb, R. M., Libanori, R., Rothfuchs, N. & Studart, A. R. Composites reinforced in three dimensions by using low magnetic gields. *Science* **335**, 199–204 (2012).
38. Liu, C. et al. Static electricity powered copper oxide nanowire microbicidal electroporation for water disinfection. *Nano Lett.* **14**, 5603–5608 (2014).
39. Bai, H. W., Liu, Z. Y. & Sun, D. D. Hierarchical ZnO/Cu 'corn-like' materials with high photodegradation and antibacterial capability under visible light. *Phys. Chem. Chem. Phys.* **13**, 6205–6210 (2011).
40. El Badawy, A. M. et al. Surface charge-dependent toxicity of silver nanoparticles. *Environ. Sci. Technol.* **45**, 283–287 (2011).
41. Gao, P., Ng, K. & Sun, D. D. Sulfonated graphene oxide-ZnO-Ag photocatalyst for fast photodegradation and disinfection under visible light. *J. Hazard. Mater.* **262**, 826–835 (2013).
42. Wang, W. J. et al. Visible-light-driven photocatalytic inactivation of *E. coli* K-12 by bismuth vanadate nanotubes: bactericidal performance and mechanism. *Environ. Sci. Technol.* **46**, 4599–4606 (2012).
43. Wang, W. J., Yu, J. C., Xia, D. H., Wong, P. K. & Li, Y. C. Graphene and g-C_3N nanosheets co-wrapped elemental α-sulfur as a novel metal-free heterojunction photocatalyst for bacterial inactivation under visible-light. *Environ. Sci. Technol.* **47**, 8724–8732 (2013).

Acknowledgements

This work was supported by the US Department of Energy, Basic Energy Sciences, Materials Sciences and Engineering Division, under contract DE-AC02-76SF00515. We acknowledge the Stanford facilities, Stanford Nanocharacterization Laboratory and Soft & Hybrid Materials for characterization. We thank A. Boehm for assistance with the biology laboratory and facilities. We thank G. Li for his help with the ICP–MS test. We also thank Y. Zhou from Shiyanjia Lab (www.shiyanjia.com) for the electron paramagnetic resonance analysis and J. Xie from Shanghai Tech University for UV photoelectron spectroscopy measurements.

Author contributions

T.W. and B.L. contributed equally to this work. T.W. and Y.C. developed the concept. T.W., B.L. and C.L. synthesized the samples and conducted the disinfection measurements and material characterizations.

T.W. completed the material synthesis. J.W. helped with the magnetic modification. A.Y. helped with the Raman measurements. K.L. and F.S. helped with the SEM and XPS measurements. Z.L. helped with the XRD measurements. J.Z. helped with the TEM measurements. G.C. analysed the data. T.W., Y.C., H.Y.H. and A.P. co-wrote the paper. All the authors discussed the whole paper.

Competing interests

The authors declare no competing financial interests. Readers are welcome to comment on the online version of the paper.

Additional information

Supplementary information The online version contains supplementary material available at https://doi.org/10.1038/s44221-023-00079-4.

Correspondence and requests for materials should be addressed to Yi Cui.

Peer review information *Nature Water* thanks the anonymous reviewers for their contribution to the peer review of this work.